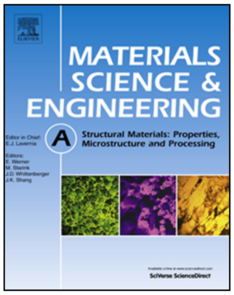

Effects of natural aging and pre-aging on the strength and electrical conductivity in Al-Mg-Si AA6201 conductor alloys

Siamak Nikzad Khangholi, Mousa Javidani, Alexandre Maltais, X.-Grant Chen

PII: S0921-5093(21)00807-8

DOI: https://doi.org/10.1016/j.msea.2021.141538

Reference: MSA 141538

To appear in: *Materials Science & Engineering A*

Received Date: 8 April 2021

Revised Date: 28 May 2021

Accepted Date: 30 May 2021

Please cite this article as: S.N. Khangholi, M. Javidani, A. Maltais, X.-G. Chen, Effects of natural aging and pre-aging on the strength and electrical conductivity in Al-Mg-Si AA6201 conductor alloys, *Materials Science & Engineering A* (2021), doi: https://doi.org/10.1016/j.msea.2021.141538.

Credit authorship contribution statement:

Siamak Nikzad Khangholi: Methodology, Investigation, Formal analysis, Writing – original draft.

Mousa Javidani: Conceptualization, Methodology, Writing – review & editing.

Alexandre Maltais: Conceptualization, Validation, Writing – review & editing.

X.-Grant Chen: Conceptualization, Validation, Writing – review & editing, Project administration.

Effects of natural aging and pre-aging on the strength and electrical conductivity in Al-Mg-Si AA6201 conductor alloys

Siamak Nikzad Khangholi [a], Mousa Javidani [a, 1], Alexandre Maltais [b], X.-Grant Chen [a]

[a] Department of Applied Science, University of Québec at Chicoutimi, Saguenay,
Québec, G7H 2B1, Canada

[b] Arvida Research and Development Center, Rio Tinto Aluminum, Saguenay, Quebec,
G7S 4K8, Canada

Abstract

The effects of natural aging (NA), and its combination with pre-aging (PA), on the strength and electrical conductivity (EC) of drawn Al–Mg–Si AA6201 conductor alloys were studied. Natural aging had a negative impact on precipitation before the drawing process. However, wire drawing counteracted the detrimental influence of natural aging on precipitation hardening; after drawing and post-aging, the NA samples exhibited a better combination of strength and EC compared to those of the samples that did not undergo NA. Transmission electron microscopy results show that the NA samples exhibited a higher number density of precipitates in the drawn and post-aged conditions relative to those of the samples that did not undergo NA. The combination of natural aging and pre-aging followed by wire drawing and post-aging provided the highest strength (369 MPa) with an acceptable EC (53% IACS). The applied natural aging and pre-aging modified the strengthening contributions in AA6201 conductor alloys in favor of precipitation hardening. The relationship between strength and EC was analyzed in detail using strengthening models and Matthiessen's rule based on various microstructural features.

Keywords: Al-Mg-Si conductor alloys, electrical conductivity, mechanical properties, natural aging, pre-aging

1. Introduction

The demand for self-supporting overhead power lines in the electrical industry has attracted broad attention for the use of Al–Mg–Si conductor alloys (such as AA6101 and AA6201 alloys) because these Al alloys provide an excellent combination of high strength with the desired electrical conductivity (EC) [1-3]. The principal strengthening mechanisms in aluminum alloys are precipitate strengthening, strain hardening, solute strengthening, and grain-boundary

---

[1] Corresponding author: mousa_javidani@uqac.ca

hardening. However, electrical resistivity originates from crystal defects, solutes, and precipitates owing to disruptions in the atomic periodicity and strain fields in a crystal structure [4-7]. Solute atoms along with GP zones are known to be strong factors that scatter conduction electrons [4, 5, 8]. Therefore, the parameters that improve the strength often cause an increase in electrical resistivity in Al–Mg–Si conductor alloys, indicating that strength and EC are mutually incompatible.

The predominant fabrication route of Al conductor cables is by means of the Properzi continuous casting–rolling (CCR) process, followed by cold wire drawing (Fig. 1) [2, 9]. A bar with a trapezoidal cross section (Fig. 1a), cast by a Properzi wheel, is directed toward an in-line multi-stand hot-rolling process to produce a rod with a diameter of 9.5 mm (Fig. 1b) [10]. The rod is subsequently cold-drawn to fabricate electrical cables (Fig. 1c). The temperature of the cast bar prior to hot rolling is maintained above the solvus temperature of the Al–Mg–Si alloy to ensure solutionizing and optimal aging response [11]. Immediately after the rolling process, the rods are rapidly cooled to 50-65 °C by spraying an oil-in-water emulsion to prevent precipitation. The rods, which are directed to the winding process in the subsequent step, require a few hours to reach room temperature [9]. The coiled rods are eventually subjected to a wire drawing process, followed by artificial aging to optimize the strength and EC [2]. As the wire drawing process is typically implemented in a separate unit, the transportation and storage arrangements normally delay the drawing process up to several weeks. The slow cooling from 50-65 °C and subsequent storage at room temperature often cause substantial natural aging before the wire drawing process. This type of natural aging in the industrial practice is slightly different as the conventional natural aging at room temperature owing to a part of aging at higher temperatures (50-65 °C).

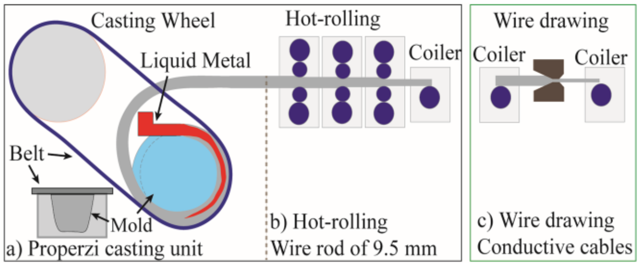

Fig. 1 Schematic Properzi process for aluminum conductive wires

Rometsch et al. [12] reported that natural aging without cold working results in the formation of numerous solute clusters and GP zones while slightly reducing the quantity of dissolved atoms in the matrix. Thus, the formation of clusters and GP zones increases the strength but decreases the EC because the radius of the clusters and GP zones is smaller than the electron mean free path [7]. In practice, natural aging takes place during storage before the wire drawing process [3, 9], meaning that wire drawing might affect the clusters and GP zones that form during natural aging. Cervantes et al. [3] reported that natural aging of the AA6201 alloy at room temperature followed by wire drawing and post-aging exhibited a better combination of strength and EC compared to those of samples that did not undergo natural aging in the subsequent aging treatment, of which the underlying microstructure was not investigated.

Several studies have been devoted to the modified thermomechanical treatment (M-TMT) with artificial pre-aging before the drawing process and post-aging to attain a better trade-off between strength and EC compared to those achieved by the conventional thermomechanical treatment [13-15]. It has been reported that the presence of precipitates in samples fabricated using the M-TMT could boost strain hardening during cold deformation [13, 15], although Cheng et al. [16] observed that the samples exposed to under-aging and peak-aging exhibited less strain hardening compared to that of the as-quenched samples. Therefore, the exact strengthening mechanisms in M-TMT samples remain controversial.

Given that precipitation hardening is one of the major strengthening factors in Al–Mg–Si alloys, it is worthwhile to address the precipitation sequence during aging treatment. The precipitation sequences of the Al–Mg–Si materials in the as-quenched condition are as follows: clusters of Mg and Si atoms, GP zones, β'', β', and equilibrium β-Mg_2Si [17, 18]. However, cold deformation after solution treatment can disturb precipitation events owing to the presence of dislocations. In deformed samples, β' precipitation can be promoted along the dislocations, and β'' precipitation might be bypassed [19-21]. Therefore, the precipitation sequences in the as-deformed condition can become clusters/GP zones, β', and equilibrium β-Mg_2Si [20, 21].

In the present work, natural aging was adopted in the thermomechanical treatment to simulate the aforementioned natural aging in industrial practice. This study focuses on the evolution of the strength and EC of naturally aged and pre-aged AA6201 conductor alloys compared to those of alloys with no natural aging. The microstructural evolution under various conditions was investigated using transmission electron microscopy (TEM) and differential scanning calorimetry (DSC) analysis. The mechanisms for improving the strength and EC of AA6201 conductor alloys are discussed based on constitutive models.

2. Experimental

An AA6201 alloy with the chemical composition of Al-0.62%Mg-0.62%Si-0.1%Fe (wt.%) was prepared in an electrical resistance furnace. The melt was cast in a steel permanent mold to obtain cast ingots with a dimension of 30 mm × 40 mm × 80 mm. After casting, the homogenization of cast ingots was conducted at 560 °C for 6 h, followed by hot rolling at 350-480°C with an area reduction of 70%. Afterward, the samples were cut and machined into the square bars. The hot-rolled materials were subjected to a solution heat treatment at 540 °C for 2h, and then water-quenched to the room temperature. The experimental procedures of natural aging and pre-aging are shown in Fig.2. As the base case for the comparison, a set of samples after wire drawing without natural aging were prepared (Fig. 2a), designated as the No-NA samples. The natural aging was composed of 10h or 20h at 70 °C followed by keeping at room temperature for 2 weeks (Fig. 2b), referred to as 10NA and 20NA samples hereafter, respectively. It should be mentioned that this type of natural aging was designed to simulate the industrial natural aging phenomenon in the lab controlled condition. Subsequently, cold wire drawing with 50% reduction was applied to the samples, producing wires with a diameter of 4.7 mm. The artificial aging at 180 °C at different aging times was applied just after wire drawing. Another set of 20NA samples was exposed to the pre-aging at 180 °C for 5h (similar to the peak-aging T6 temper), labeled as 20NA-PA samples. Then it followed by the wire drawing (50% reduction) and re-aging at different times (Fig. 2c).

The mechanical properties of drawn wires were characterized by microhardness and tensile strength. The HV hardness tests were carried out on the cross-sectional surfaces of the samples perpendicular to the wire drawing direction with a constant force of 25 g and dwell time of 20 s. The reported hardness value was based on an average of at least eight measurements. Tensile tests were conducted on the samples with a gage length of 250 mm at the strain rate of 8×10^{-4} s^{-1} according to ASTM B557 and ASTM E8. For each condition, three tensile tests were performed, and the mean strengths were reported. The electrical conductivity was determined by at least fifteen measurements using the Sigmascope method with a frequency of 480 kHz based on ASTM E1004.

Differential scanning calorimetry (DSC) analysis was performed by the PerkinElmer machine in an argon atmosphere with a heating rate of 10 ^{o}C/min to reveal the precipitation behavior of the samples. The measurement of classical onset and peak temperatures was carried out based on the technique described in Ref. [22]. The precipitates and dislocations were analyzed using TEM operated at 200 kV. TEM samples were mechanically ground and then electropolished by a twin jet unit with the solution of 30% HNO_3 in methanol at the temperature between -20 and -30°C. The foil thickness was measured by the convergent beam electron diffraction (CBED) technique. The bright-field TEM images were acquired in <001> zone axis for precipitates and in <011> zone axis for dislocation observation. The methods for precipitate statistics were elaborated in detail in Ref. [23]. The average precipitate length was measured (at least for 200 precipitates) in <200> and <020> zone axis using the image analyzer software (Image J) on TEM micrographs. The measured precipitate length was corrected based on the tilting in X and Y direction and then reported. In addition, the average cross section of precipitates was also measured (at least for 200 precipitates) in <002> zone axis using the same software (Image J) on TEM micrographs. The final equation to measure the precipitate density is defined as follows [23].

$$\rho = \frac{3N}{A(t+\lambda)} \qquad (1)$$

Where N, A, t and λ stand for the number of precipitates in <001> zone axis, area of the matrix containing the precipitates, foil thickness on which precipitates are observed, and the corrected average precipitate length, respectively.

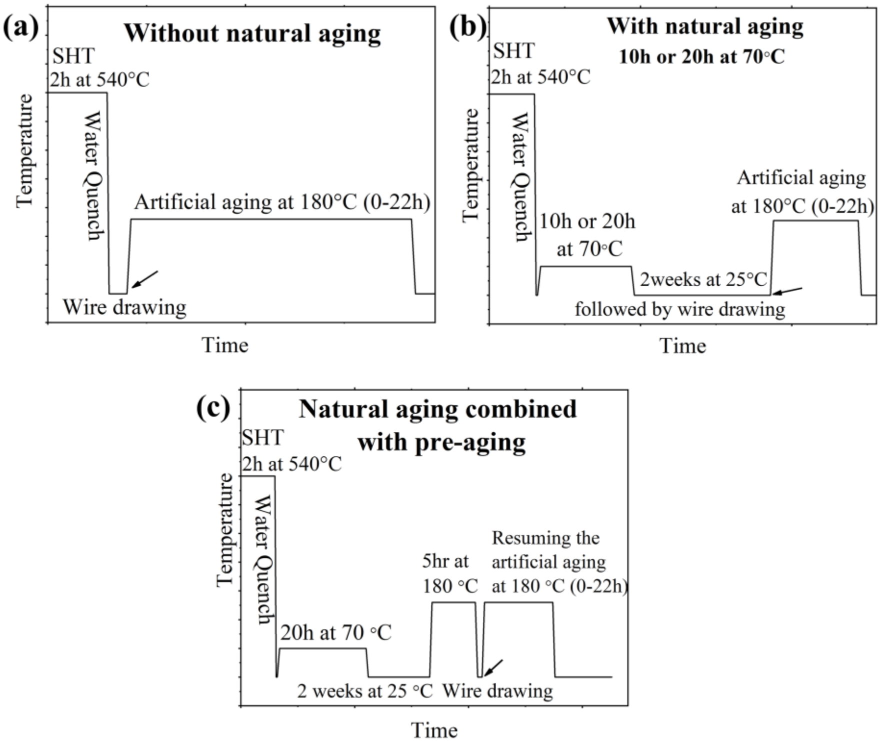

Fig. 2 A scheme of the experimental procedures (a) without natural aging (b) with natural aging (c) natural aging combined with pre-aging. Arrows show where wire drawing was applied

3. Results

3.1. Strength and EC

Fig. 3a and 3b show the evolution of hardness and EC during artificial aging at 180 °C, respectively. The hardness curves (Fig. 3a) indicate that the peak hardness of the samples with natural aging (10NA or 20NA samples) was higher than that of the No-NA samples. The hardness of the No-NA, 10NA, and 20NA samples reached 128, 133, and 138 HV, respectively, under the peak-aged condition. After peak aging, the hardness of all the samples gradually decreased with aging time. The No-NA samples reached the peak hardness in a shorter aging time compared to those of the 10NA and 20NA samples. Overall, the 20NA-PA samples exhibited the highest hardness values at a given aging time. Given that the 20NA-PA samples reached the peak hardness before wire drawing with pre-aging at 180 °C for 5 h, its hardness after wire drawing continuously decreased with aging time, as presented in Fig. 3a.

Fig. 3b shows that the EC values for the naturally aged materials and the No-NA samples grew sharply in the early stage of aging owing to the decomposition of the supersaturated samples and then moderately increased until reaching a plateau. Although the EC values of the 20NA-PA samples improved during the pre-aging treatment to some extent, their increased EC values during the early stage of aging were less than those of the other sample conditions. Therefore, the 20NA-PA samples possessed the lowest EC at a given aging time above 5 h of aging. The EC improvement during post-aging can most probably be attributed to the extraction of solutes into precipitates because the electrical resistivities of precipitates are less than those of solutes.

The hardness and EC of the non-drawn 20NA samples are also shown in Fig.3a and b for the comparison. The non-drawn 20NA samples reached the peak hardness after 5h aging, showing low precipitation kinetics due to the small number of dislocations. In addition, its EC values increased more slowly relative to the drawn samples, suggesting that dislocations could assist the extraction of more solutes into precipitates and resulting in higher EC in the drawn samples.

Fig. 3c shows the hardness versus EC for all aging times, and Fig. 3d shows an enlarged view of the hardness and EC above 52.5% IACS, which is the minimum required EC for AA6201 conductor alloys [24]. As shown in Fig. 3c, the non-drawn 20NA samples did not exceed the minimum required EC. Fig. 3d reveals that the 10NA, 20NA, and 20NA-PA samples outperformed the No-NA samples in terms of hardness and EC. The hardness of the 20NA-PA sample was superior to that of the other samples by up to 53% IACS. However, the surplus of the 20NA-PA samples reduced with a further increase in % IACS, resulting in a rather narrow window of EC and hardness above 52.5% IACS. In general, if the strength is the main concern, the 20NA-PA material (with the minimum 52.5% IACS) is an appropriate choice for conductor alloys. However, the 10NA and 20NA materials show a better combination of strength with EC when a high EC (above 53% IACS) is the priority.

Because the principal objective of this study was to improve strength while satisfying the minimum required EC, according to the results presented in Fig. 3, the samples aged for 5 h were chosen for further tensile tests. The ultimate tensile strength (UTS) values for the No-NA, 10NA, 20NA and 20NA-PA samples were 332, 339, 343, and 369 MPa, respectively, as shown in Fig. 4a along with their EC values. The NA samples exhibited a relatively higher strength than that of the No-NA samples. The 20NA-PA sample had the highest strength, while the No-NA samples showed the lowest strength among all studied samples above the minimum required EC. Fig. 4b shows a comparison of the UTS values of the present work with the materials (AL2 to AL7) referred to in the EN 50183 standard [26]. It is apparent that the strengths of all samples studied were above the requirements of the EN 50183 standard [24] for Al–Mg–Si cables with the conventional thermomechanical treatment. Comparing the 20NA-PA sample after 5 h of aging with AL3 at ~53% IACS, it can be deduced that the strength was improved by approximately 25% in the present work.

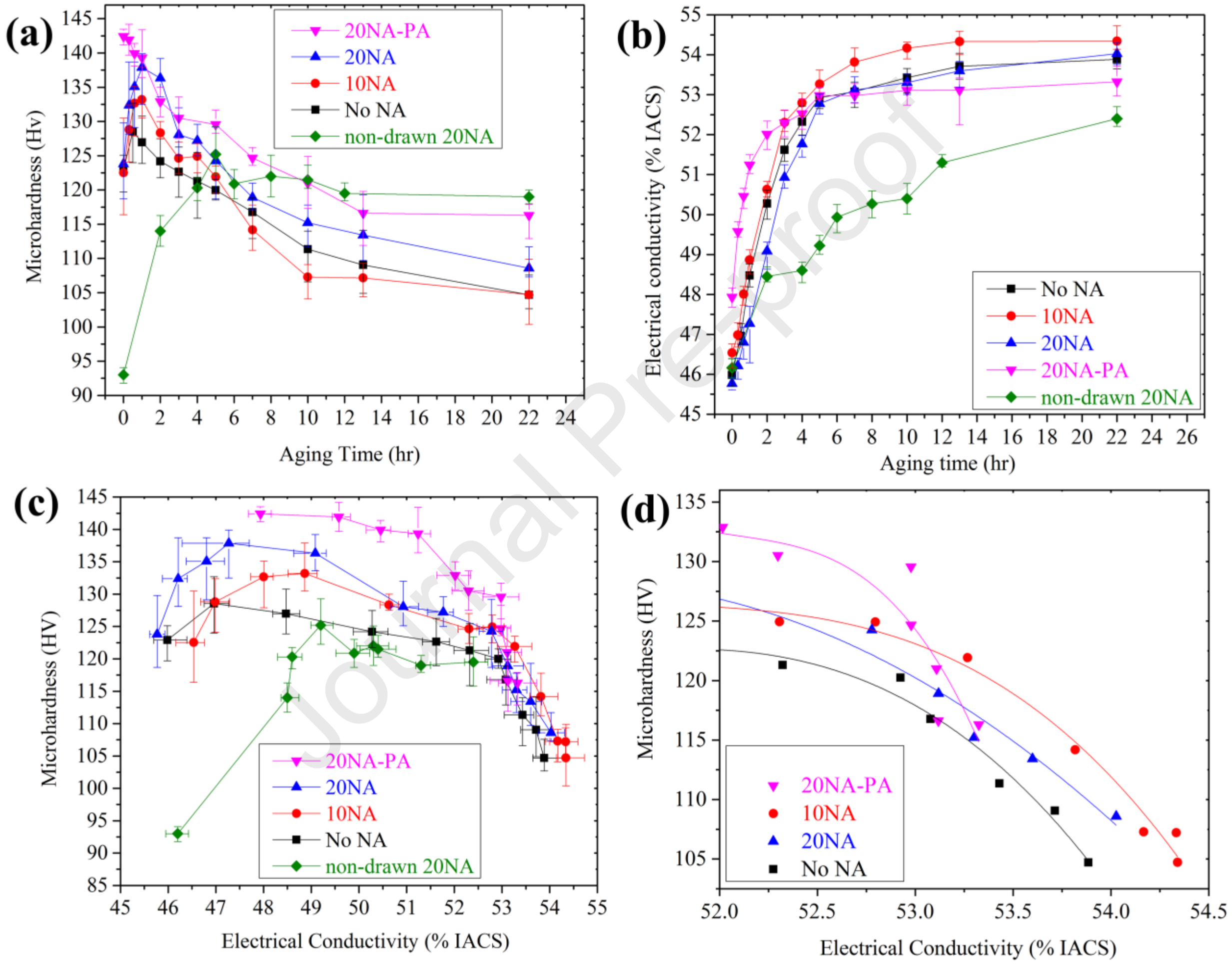

Fig. 3 Evolution of (a) HV hardness and (b) EC as a function of the aging time, (c) HV hardness as a function of EC for all aging times and (d) enlarged HV hardness as a function of EC above 52 % IACS. Error bars are omitted for the clarity in Fig. 3d.

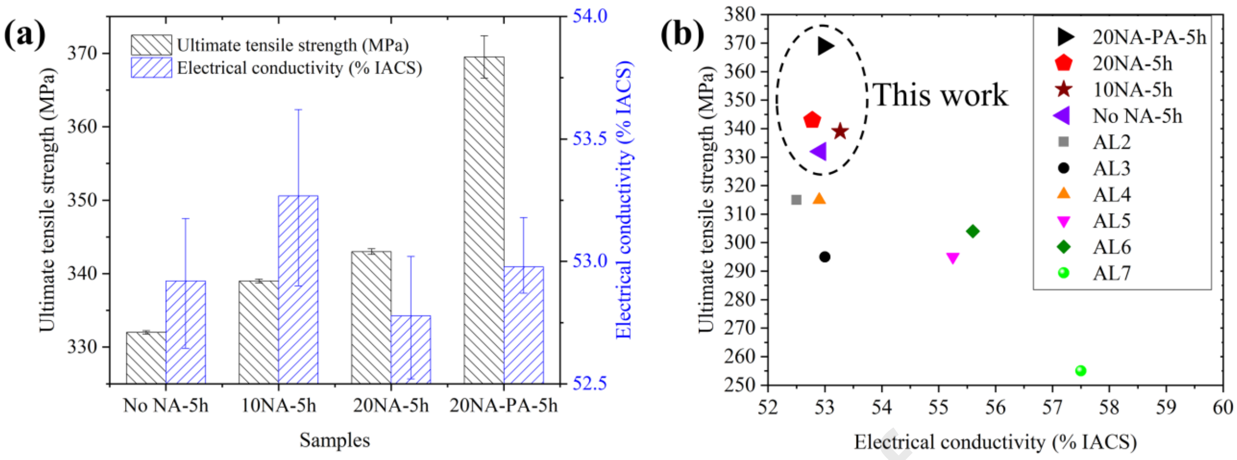

Fig. 4 (a) the ultimate tensile strengths above 52.5 %IACS along with their EC values and (b) comparison of the ultimate tensile strengths of the present work with the materials referred in EN 50183 standard [24] for the ø4.7 mm wires.

3.2. DSC analysis

Fig. 5 shows the results of the DSC analysis of the samples under various natural aging conditions. As shown in Fig. 5a, the DSC curves of the samples prior to wire drawing revealed three main exothermic peaks (I, II, and III), which correspond to the formation of β", β', and β precipitates, respectively. This is consistent with the conventional precipitation sequence of these alloys [18]. Considering that the β" precipitates are the major strengthening phase in Al–Mg–Si 6xxx alloys [18], a closer look at peak I of the three materials is shown in Fig. 5b. The onset temperatures of peak I for the No-NA, 10NA, and 20NA samples were 239, 244, and 243 °C, whereas the peak temperatures were 265, 267, and 266 °C, respectively. It can be deduced from the onset and peak temperatures that natural aging relatively retarded β" precipitation before wire drawing, which most likely resulted from more vacancy consumption in the NA samples. Given that the area encompassed under peak I is proportional to the quantity of β" precipitates, it is clear from Fig. 5b that natural aging caused a notable decrease in the amount of precipitation relative to that of the freshly quenched sample (No-NA). Consequently, the AA6201 alloy was sensitive to natural aging, and natural aging was found to be detrimental prior to the drawing process.

Fig. 5c displays the DSC results of the samples under the as-drawn condition. It is evident that two exothermic precipitation peaks appeared after wire drawing. Heavy deformation prior to the aging treatment could disrupt early precipitation and modify the precipitation sequence. The DSC results indicate that β" precipitation was suppressed, and β' precipitation was promoted along the dislocations in the drawn samples, as reported in Ref. [19-21]. In deformed samples, it has been reported that the I_d peak might be associated with the concurrent formation of needle-shaped and lath-like precipitates, whose crystal structures are similar to that of the β' phase. The exothermic II_d peak has been attributed to the precipitation of the β phase [19-21]. These β'-type precipitates serve as the principle strengthening phase after wire drawing. The close view of the I_d peaks in Fig. 5d reveals that the onset temperatures of the I_d peak for the drawn No-NA, 10NA, and 20NA samples were 213.1, 214.2, and 214.3 °C, while the peak temperatures were 238.1, 243.7, and 243.7 °C, respectively. It can be inferred that natural aging led to an increase in the onset and peak temperatures for the I_d peak. This is consistent with the relatively longer aging time required to reach peak hardness for the naturally aged samples compared to that of the No-NA sample (Fig. 3a). The relatively large areas of the I_d peaks in the naturally aged samples (10NA and 20NA) indicates that the strengthening precipitates were promoted with natural aging in the as-drawn state (Fig. 5d), which is consistent with the higher peak hardness of the naturally aged samples compared to that of the No-NA samples. When comparing the DSC results before and after wire drawing, it can be concluded that heavy deformation (cold wire drawing) could suppress the adverse effect of natural aging on the strengthening precipitates.

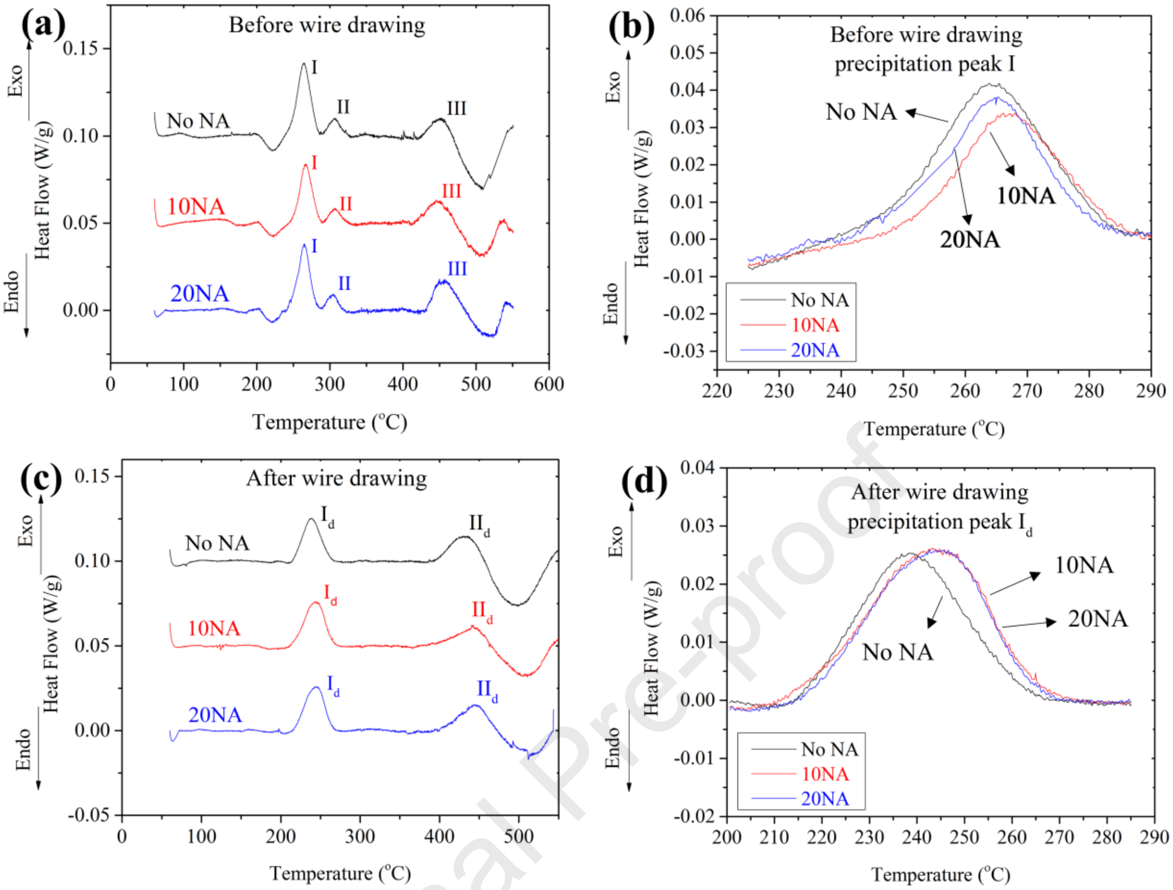

Fig. 5 DSC curves of the samples under different natural aging conditions, (a) before wire drawing, (b) a close view of peaks I in Fig. 5a, (c) after wire drawing and (d) an enlarged view of peaks I_d in Fig. 5c.

3.3. TEM microstructural analysis

To correlate the mechanical strength and precipitates, TEM micrographs of the No-NA, 20NA, and 20NA-PA samples aged at 180 °C for 5 h are shown in Fig. 6. As mentioned previously, the EC values of these samples were higher than 52.5% IACS. All precipitates were oriented in the <200> Al direction, and the dark point-like spots were cross sections of precipitates directed along the [002] Al direction. The number densities of the precipitates are shown in Fig. 6d, and the mean precipitate lengths along with their cross-sectional area are shown in Fig. 6e. The precipitates in the No-NA and 20NA samples were identified as the β'-type phase according to the morphology of the precipitates as well as the above DSC results [19-21]. The 20NA sample aged for 5 h possessed a higher number density of precipitates relative to the No-NA sample aged for 5 h, resulting in higher hardness values at a given EC (Fig. 3d). The 20NA-PA sample aged for 5 h exhibited the highest precipitate number density among all samples, leading to the largest precipitate strengthening contribution (Fig. 3d). The precipitates in the 20NA-PA samples aged for 5 h were evenly dispersed throughout the matrix (Fig. 6c). The average cross section and, most notably, the length of the precipitates in the 20NA-PA sample were much smaller than those in the 20NA and No-Na samples. The results in Fig. 6e also show that the mean cross section of precipitates in the No-NA and 20NA samples were more or less similar, whereas the precipitate length in the 20NA sample was relatively smaller.

Fig. 7 shows a closer observation of the precipitates for three different samples: the No-NA sample at peak aging, the No-NA sample aged for 5 h, and the 20NA sample aged for 5 h. In the peak-aged No-NA sample, the precipitates were identified with their cross-sectional projections (laths and needles) extending in the <001> Al direction (white arrows in Fig. 7a), in which coarse lath-like precipitates along dislocations and needle-shaped precipitates were observed. The crystal structures of these precipitates were similar to that of the β' phase, as reported in Ref. [19, 20]. As mentioned previously, cold deformation (drawing) can modify the precipitation sequence by suppressing the formation of the β" phase [19-21], as confirmed by the DSC results in Fig. 5. The lath-like precipitates extended along the dislocation line and were dominant in the microstructure (Fig. 7a). After 5 h of aging, the precipitates in the No-NA sample coarsened (Fig. 6a and Fig. 7b) and were randomly distributed, as shown in Fig. 7b with white arrows. In addition to the same precipitates as those observed in the No-NA sample aged for 5 h, the 20NA sample aged for 5 h had a considerable number of precipitates with a smaller cross section, as indicated by the white arrows in Fig. 7c. These fine precipitates also extended in the <001> Al direction and were distinguishable from the coarse lath-like precipitates owing to their smaller cross section. The distribution of these fine precipitates was unrestrained by dislocations. The higher precipitate number density (Fig. 6d) and higher hardness values (Fig. 3a) in the 20NA sample compared to those of the No-NA sample after 5 h of aging could stem from the presence of these precipitates.

Fig. 8 shows the evolution of precipitates in the 20NA-PA samples before and after wire drawing. Before wire drawing, a large number of precipitates were observed in the 20NA-PA sample (Fig. 8a). After wire drawing, the precipitate length and cross-sectional area decreased considerably (Fig. 8b and 8e), while the precipitate number density decreased slightly (Fig. 8d). The re-dissolution of some β" precipitates was plausible during wire drawing, as reported in Ref. [25]. Based on the size of the precipitates (~30 nm) in the 20NA-PA sample before wire drawing, it can be concluded that the majority of precipitates were shearable β" precipitates [26]. The dislocations generated through drawing could consecutively shear the pre-existing β" precipitates in the 20NA-PA samples, resulting in small fragmented precipitates; precipitate fragmentation has also been reported via dislocation sliding in plastic deformation in Ref. [5, 27, 28]. After re-aging the drawn 20NA-PA samples for 5 h to obtain the desired EC, the precipitates became coarser, and their number density decreased (Fig. 8c and 8d).

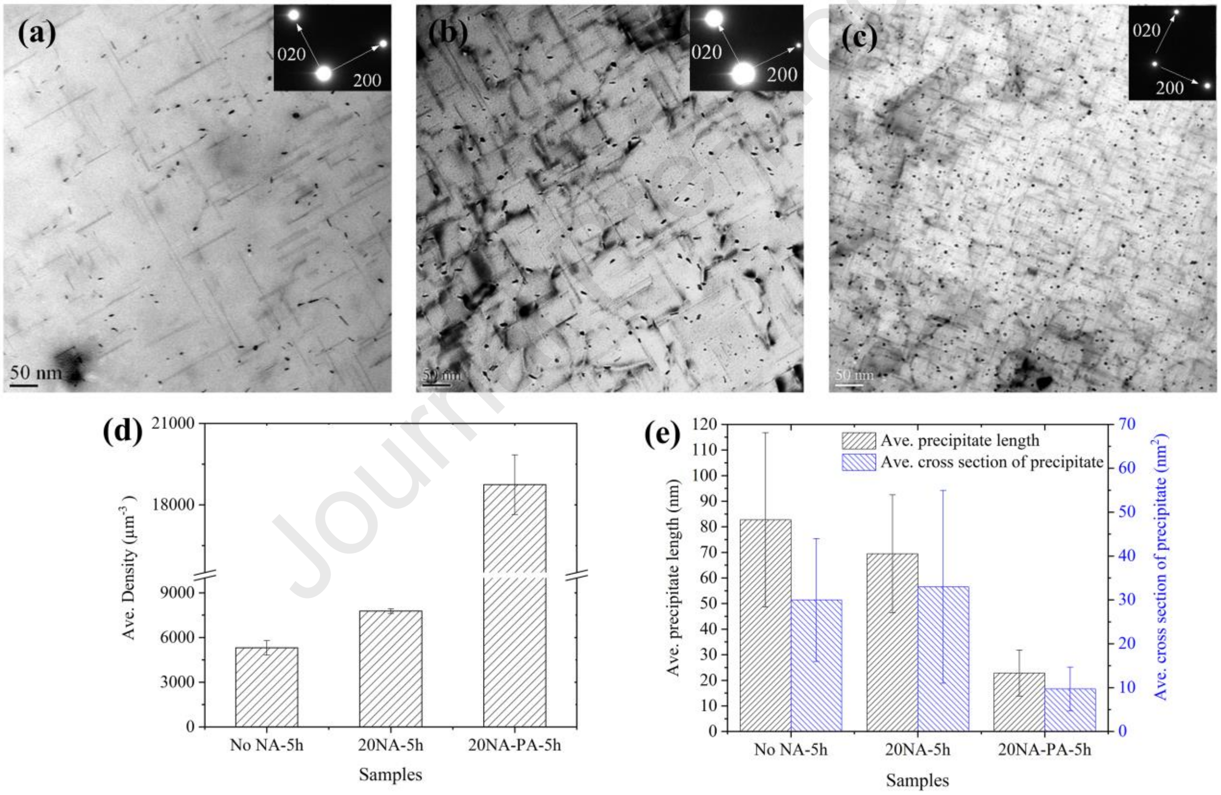

Fig. 6 Bright-field TEM micrographs of (a) No-NA sample after 5 h aging (b) 20NA sample after 5 h aging (c) 20NA-PA sample after 5 h aging, (d) the number density of precipitates and (e) the average length and the cross section of precipitates.

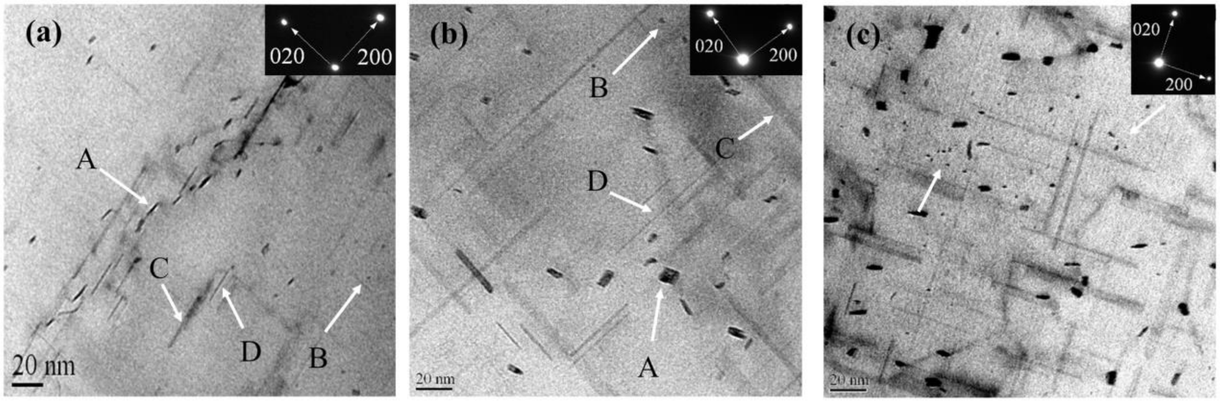

Fig. 7 (a) precipitates formed along the dislocations in No-NA sample at peak aging condition, (b) No-NA sample aged for 5 h, and (c) 20NA sample aged for 5 h. A and B correspond to the cross-sectional projections of lath-like and needle-shaped precipitates in <002> direction; C and D correspond to the longitudinal projections lath-like and needle-shaped precipitates, respectively.

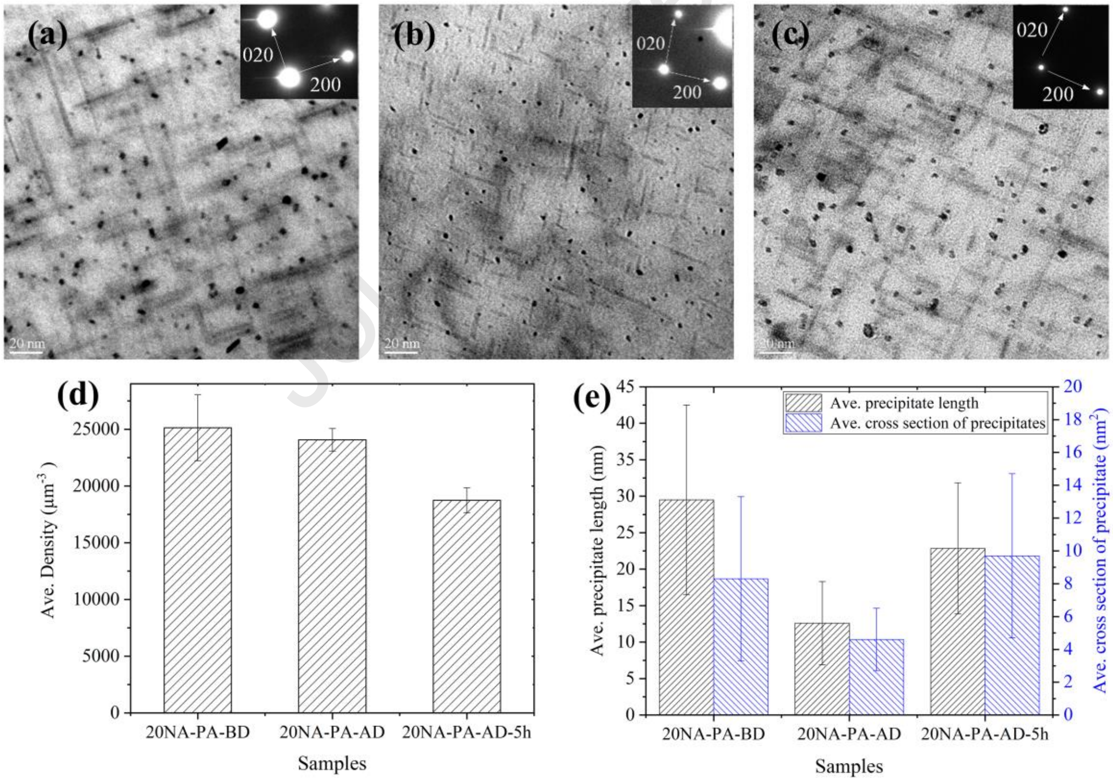

Fig. 8 Bright-field TEM micrographs of 20NA-PA samples (a) before wire drawing, (b) after wire drawing, (c) after wire drawing and 5 h aging, (d) the precipitate number density and (e) the average precipitate length and their cross section.

3.4. Strain hardening contribution

In general, strain hardening is one of the main strengthening mechanisms in Al–Mg–Si conductor alloys. The contribution of strain hardening to strengthening was determined by measuring the difference in hardness before and immediately after wire drawing without aging. The increased hardness values due to wire drawing for the No-NA, 20NA, and 20NA-PA samples were 28.6, 29.3, and 16.7 HV, respectively, as shown in Fig. 9. It was found that aging at 180 °C had a small effect on the recovery softening in the drawn aluminum. From Fig. 9, it appears that the 20NA-PA sample exhibited the least strain hardening among all samples, although a higher flow stress was required to perform the drawing [29]. In fact, the strain hardening contribution in the No-NA and 20NA samples was similar and almost double that of the 20NA-PA sample. It is apparent that alloying elements in solid solution led to higher work hardening (in the No-NA and 20NA samples) relative to alloying elements in the form of precipitates (in the 20NA-PA sample), which is in broad agreement with Ref. [16, 25]. This can be attributed to the drag effects of solutes on the dislocations in the No-NA and 20NA samples [16].

Fig. 10 shows TEM micrographs of the drawn samples aged for 5 h, revealing the dislocation structures. TEM images were taken in the <011> zone axis close to the (111) planes because the (111) planes are major dislocation slip planes in face-centered cubic aluminum alloys. As observed in Fig. 10, dislocations were entangled in all the samples after the drawing process. In addition to dislocation tangle, some well-defined dislocation cells were also found in the No-NA and 20NA samples, as indicated by the white arrows in Fig. 10a and 10b, where the walls consisted of entangled dislocations. The well-defined dislocation cells were most likely formed in the samples with a higher number of dislocations (20NA and No-NA samples) [30].

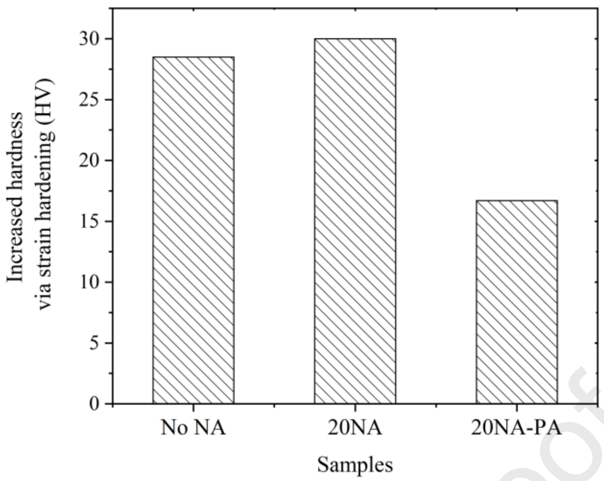

Fig. 9 The hardness increments via strain hardening from wire drawing in three samples.

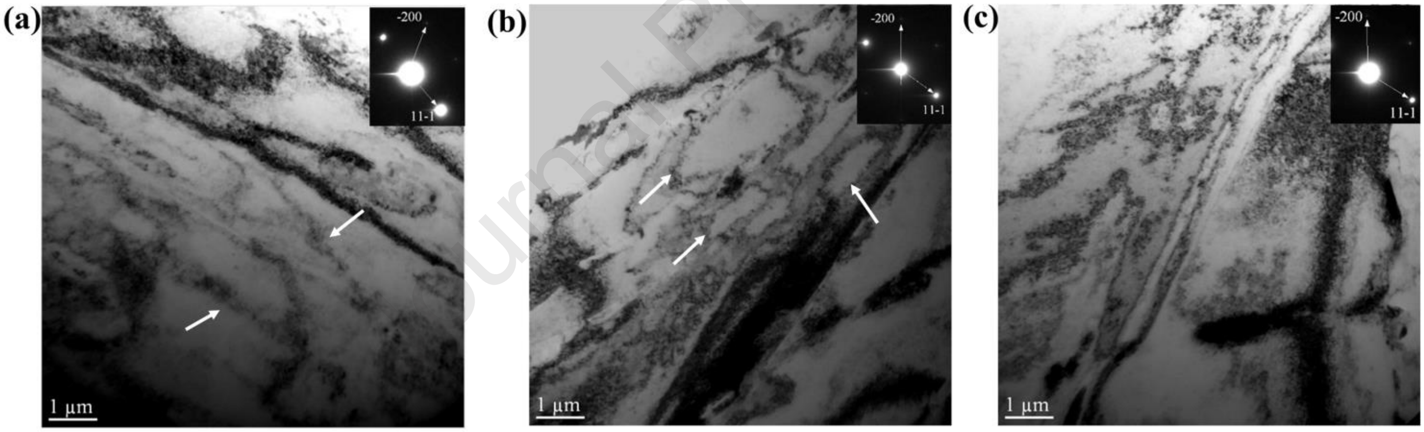

Fig. 10 The dislocation cell substructures for (a) No-NA ; (b) 20NA ; (c) 20NA-PA samples after 5 h aging taken from <011> zone axis close to (111) planes.

4. Discussion

4.1. Constitutive modeling for strength and EC

In heat-treated and deformed Al–Mg–Si alloys, several strengthening mechanisms are operative, including precipitate strengthening, solid-solution strengthening, dislocation hardening, and grain-boundary hardening. For the mechanical strength, the HV hardness of conductor materials in a given state can be simulated with the aid of different strengthening mechanisms and the corresponding constitutive equations, assuming that the contributions of the strengthening mechanisms are independent and can be added in a linear manner. It is also assumed that the yield stress is three times the hardness ($\Delta\sigma \approx 3 \times \Delta HV$) [4, 6, 31]. Then, the estimated hardness values can be compared with the experimental values. The total hardness in terms of the hardness values from the various strengthening factors can be expressed as follows:

$$HV_{total} = HV^{Al} + \Delta HV^{dislo} + \Delta HV^{prec} + \Delta HV^{gb} + \Sigma\Delta HV_i^{sol} \qquad (2)$$

Where the total hardness (HV_{total}) is estimated by summing the hardness contribution from each component, including the aluminum matrix (HV^{Al}), the dislocation forest via strain hardening in the cold wire drawing (ΔHV^{dislo}), the flow stress contributions due to precipitates (ΔHV^{prec}), grain boundaries (ΔHV^{gb}) and the solid solution solutes ($\Sigma\Delta HV_i^{sol}$) [4, 6]. The yield stress of the aluminum matrix is in the order of 35 MPa for an annealed pure 1100-O aluminum alloy [32], and hence, HV^{Al} is considered of the order of 12 HV.

The dislocation number density in an annealed aluminum material (solution treated) is only 10^{10}-10^{11} m^{-2}, which has a negligible contribution to the hardness [23]. Therefore, the multiplication of dislocations mainly occurred during cold wire drawing. As mentioned previously, the increased hardness values due to cold drawing were directly obtained from the hardness difference before and after wire drawing (28.6, 29.3, and 16.7 HV for the No-NA, 20NA, and 20NA-PA samples, respectively). The Bailey–Hirsch equation (Eq. 3) can provide an approximation of the dislocation number density for the samples [8].

$$\Delta\sigma^{dislo} = \alpha.M.G.b.\rho^{1/2} \qquad (3)$$

Where ρ is the number density of dislocations, α is a geometric constant close to 0.3 [8], M as Taylor factor is taken as 2 to convert shear stresses into normal stresses [33], G is the shear modulus (26.9 GPa) of FCC Al, and b is the burger vector (0.29 nm) of the dislocations in FCC $Al_{(110)}$ [8]. Therefore, calculations showed that the dislocation number densities were 3.4×10^{14}, 3.5×10^{14}, and 1.1×10^{14} m^{-2} for No-NA, 20NA, and 20NA-PA samples, respectively, which was well agreed with the data in Ref. [8, 34].

Eq. 4 (Orowan equation) and Eq. 6 can be used to estimate precipitate strengthening for non-shearable β' [8] and shearable β'' precipitates [23], respectively.

$$\Delta\sigma_{Or}^{prec} = \frac{2M\beta Gb}{L} \tag{4}$$

Where β is a constant close to 0.28. M, G and b were described above. L is defined as the mean particle spacing, expressed in the following equation [8].

$$L = \frac{1}{(N)^{1/3}} \tag{5}$$

Where N is defined as precipitate number density.

$$\Delta\sigma_{shear}^{prec} = \frac{M}{b^2\sqrt{\beta G}}\sqrt{N.r}.F^{3/2} \tag{6}$$

$$F = 2\beta Gb^2.\left(\frac{r}{rc}\right) \tag{7}$$

Where r is the precipitates size (radius), r_c is the transition radius from precipitate shearing to bypassing (5nm), and F is the mean obstacle strength provided by precipitates [23].

Because the precipitates were principally non-shearable β' precipitates in the No-NA and 20NA samples, the Orowan equation (Eq. 4) was used to estimate the amount of precipitation hardening [8]. Accordingly, the average inter-precipitate spacings for the No-NA and 20NA samples aged for 5 h were 57.3 and 50.5 nm, and their hardness contributions were 50.8 and 57.7 HV, respectively.

For the 20NA-PA sample, the average precipitate length was in the range of the shearable β'' precipitates. However, using Eq. 6 for shearable precipitates, the precipitate strength was calculated to be ~15 MPa (5 HV), which far underestimated the experimental data. It appears that the nature of precipitates in the 20NA-PA sample might not be well identified based on their length because the precipitates were primarily fragmented during wire drawing and then coarsened in the over-aged state. It is worth mentioning that the hardness and precipitate number density decreased by ~10 HV and ~6000 μm^{-3}, respectively, during post-aging. It is reasonable to assume that non-shearable precipitates were the dominant feature, and the Orowan equation (Eq. 4) could still be used to estimate the amount of precipitate strengthening. The mean inter-precipitate spacing and the precipitate hardness contribution were 37.6 nm and 77.4 HV, respectively, which agree well with the experimental data.

The classical Hall–Petch relationship can be employed to estimate the hardness contribution from grain-boundary strengthening [8].

$$\Delta HV^{gb} = k_{HP}d^{-1/2} \tag{8}$$

Where HV_{gb} is the hardness induced by grain boundaries, and k_{HP} is a scaling constant taken as 35 HV $\mu m^{1/2}$ for Al–Mg–Si aluminum alloys [8]. A comparison of the grain structure of the samples revealed that the grain sizes of all samples were similar (on the order of 130 μm) because they underwent the same fabrication process. The coarse grain structure indicates that grain-boundary strengthening is only a small portion (~3 HV) of the total strength and can be assumed to be similar in all samples.

Solid-solution strengthening is generally ascribed to the interaction of dislocations with their surrounding solute atoms, resulting in pinning of the dislocations. Therefore, further external stress is required to unpin the dislocations from the solute regions [23]. Eq. 9 provides the approximate strength contribution from solid-solution strengthening [8].

$$\Delta\sigma_i = k_i C_i^{2/3} \tag{9}$$

where $\Delta\sigma_i$ is the strengthening contribution of solute i, k_i is a scaling factor for solute i ($k_{Mg} \approx$ 29 and $k_{Si} \approx$ 66.3 MPa $(wt.\%)^{-2/3}$), and C_i is the concentration of solute i (in wt.%) [4, 8]. It was found that almost half of the Si remained in the matrix in 6xxx series alloys with a Mg/Si ratio of one when aged at 175 °C for 8 h, while most of the Mg was used in the precipitates [35]. Therefore, half of the Si solutes (0.31 wt.% Si) and 0.1 wt.% Mg could remain in the matrix of the present alloy, yielding a hardness contribution of ~12 HV from solid-solution strengthening.

Fig. 11 shows a comparison of the experimentally measured hardness with the predicted hardness for various sample conditions. Although the predicted hardness was slightly lower than the measured values, the general trend of the hardness difference under various conditions agreed well with the measured total hardness. In our previous work, we found that an increase in the Si concentration (from 0.4 to 0.89 wt.%) in Al–Mg–Si alloys led to a strength increase of ~90 MPa (~25 HV) in the as-quench state before wire drawing, while the constitutive equation predicted only ~25 MPa (~8 HV) [36]. Therefore, the amount of solid-solution strengthening might be underestimated in the strength model owing to the difficulties in experimentally determining the amounts of various solutes in the matrix. As mentioned previously, the hardness contributions of solid-solution strengthening and grain-boundary strengthening were assumed to be constant in all samples, yielding a total hardness contribution of 15 HV. Accordingly, strain and precipitation hardening are the most important contributors, exhibiting the largest contributions to the overall hardness of the samples. As presented in Fig. 11, both the No-NA and 20NA samples aged for 5 h exhibited almost the same amount of strain hardening. Therefore, the higher hardness of the 20NA sample relative to that of the No-NA sample after 5 h of aging is attributed to the larger contribution of precipitation strengthening in the 20NA sample.

Although the 20NA-PA sample aged for 5 h had the highest hardness above 52.5% IACS, its strain-hardening contribution was the lowest among all samples. It can be deduced from the results in Fig. 11 that the higher strength of the 20NA-PA sample after 5 h of aging can be ascribed to the appreciably large contribution of precipitation hardening, which was approximately 50% and 35% higher than those of the No-NA and 20NA samples, respectively.

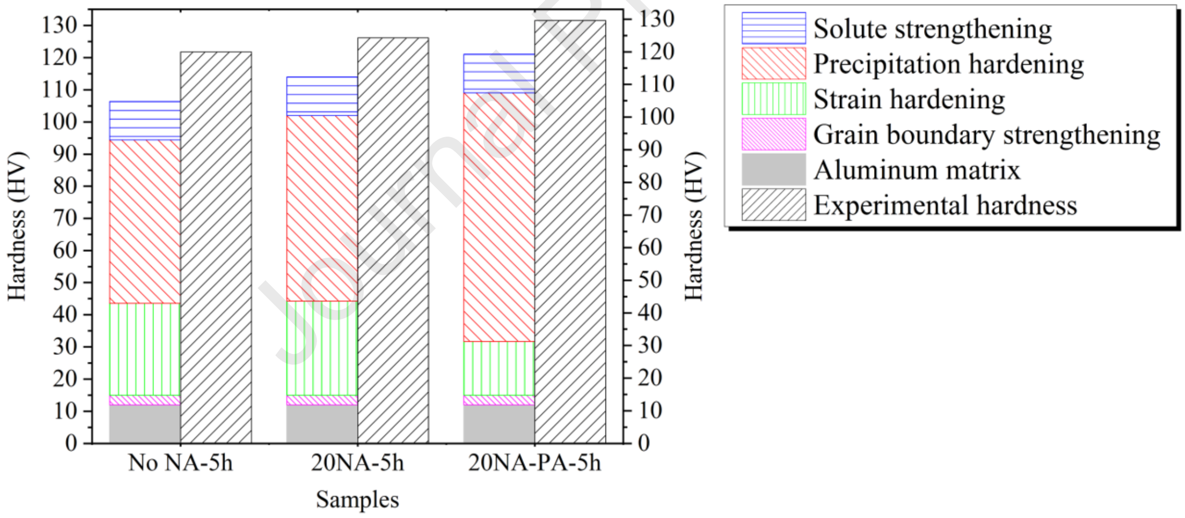

Fig. 11 The comparison between predicted and experimentally measured hardness for the No-NA, 20NA, and 20NA-PA samples aged at 180 °C for 5 h.

It is well known that most strengthening mechanisms cause distortions in the lattice structure of metals. It is assumed that each strengthening mechanism induces an additional increase in the electrical resistivity of metals. To understand the effect of the microstructural features on the EC of the conductor materials, Matthiessen's rule is adopted here (Eqs. 10 and 11), in which the total electrical resistivity is the sum of the contributions from various microstructural features (defects) that cause electron scattering [8, 37]. Then, the total EC (% IACS) can be obtained from the electrical resistivity (Eq. 12) [38].

$$\rho_{total} = \rho^{Al\ pure} + \rho^{DISLO} + \rho^{GB} + \rho^{PREC} + \rho^{SOL} \tag{10}$$

$$\rho_{(total)} = \rho^{Alpure} + L^{dislo}\Delta\rho^{dislo} + S^{GB}\Delta\rho^{GB} + \frac{\Delta\rho^{Prec}}{(L^{prec})^{1/2}} + \Sigma C_i^{sol}\Delta\rho_i^{sol} \tag{11}$$

$$\mathrm{EC\ (\%IACS)} = \frac{172.4}{\rho(\mathrm{total})\ (\mu\Omega\mathrm{cm})} \tag{12}$$

Where $\rho_{(total)}$ is the total electrical resistivity; (ρ^{Alpure}) is the electrical resistivity of AA1350–O alloy, which is 2.79×10^{-6} Ω cm at room temperature (equivalent to 61.8 %IACS) [39]; and $\Delta\rho^{dislo}$, $\Delta\rho^{GB}$, $\Delta\rho_i^{sol}$, and $\Delta\rho^{prec}$ are the resistivity constants describing for the dislocations, grain boundaries, solute elements, and precipitates in the aluminum matrix, respectively. $\Delta\rho^{dislo}$ and $\Delta\rho^{GB}$ were defined to be 2.7×10^{-25} Ωm^3 and 2.6×10^{-16} Ωm^2, respectively [8]. L^{dislo} and S^{GB} are described as the dislocation density and the portion of grain boundaries, in which S^{GB} is defined as 6/d (d is the average grain size).

As mentioned above, all samples exhibited a similar grain structure and size, giving rise to the same electrical resistivity (1×10^{-9} Ω cm), which was much smaller than the resistivity of pure Al (ρ^{Alpure}). By referring to the dislocation number density in all samples, the portions of electrical resistivity from dislocations for the No-NA, 20NA, and 20NA-PA samples were estimated to be 9.2×10^{-9}, 9.5×10^{-9}, and 3×10^{-9} Ω cm, respectively. Although the 20NA and No-NA samples exhibited a larger portion of the electrical resistivity due to the denser dislocation forest relative to that of the 20NA-PA sample, the dislocation contribution to resistivity for all samples was considerably smaller than ρ^{Alpure}. Considering the total electrical resistivity of all materials to be 3.25×10^{-6} Ω cm (equivalent to 53% IACS), it can be deduced that the electrical resistivity of the samples was less dependent on dislocations and grain boundaries. Raeisinia et al. [7] developed an equation showing the contribution of precipitates to resistivity based on the precipitate spacing, as shown in Eq. 11. For the contribution induced by precipitates, $\Delta\rho^{Prec}$ was reported to be 12 Ω $(nm)^{3/2}$, and L^{Prec} (in nm) represent the precipitate spacing in Eq. 11 [7]. Therefore, the precipitate resistivity contributions of the No-NA, 20NA, and 20NA-PA samples (aged for 5 h) were calculated to be 0.158×10^{-6}, 0.169×10^{-6}, and 0.195×10^{-6} Ω cm, respectively, which were 5%-6% of the total electrical resistivity.

In Eq. 11, C_i^{sol} is the concentration of solute (i) in the matrix, and $\Delta\rho^{Mg\ sol}$ and $\Delta\rho^{Si\ sol}$ are defined as 0.445×10^{-6} and 0.496×10^{-6} Ω cm $(at.\%)^{-1}$, respectively [8]. The electrical resistivity from Si and Mg solute atoms was estimated to be 0.193×10^{-6} Ω cm, assuming the Mg and Si solute levels mentioned above. From the above analysis and calculation, it is evident that the solutes in the matrix were the primary cause of the increase in electrical resistivity, and the precipitates with a given particle spacing were the second cause of electron scattering in the studied samples.

Using Eqs. 10 and 11, the total electrical resistivities of the No-NA, 20NA, and 20NA-PA samples were calculated to be 3.151, 3.162, and 3.182 μΩ cm, respectively. Accordingly, the EC levels calculated using Eq. 12 for the No-NA, 20NA, and 20NA-PA samples were 54.7%, 54.5%, and 54.2% IACS, respectively, which are only slightly overestimated compared to the measured EC (~53% IACS) for all samples. The calculated hardness values (Eq. 2) and EC values (Eqs. 10 and 12) are concurrently plotted in Fig. 12 and compared to the experimentally measured values for all samples. The comparison with the experimental data suggests that model captures the general trend of the hardness/EC relationship fairly well. The slightly lower hardness and higher EC values estimated by the model relative to the measured values might stem from some errors in the solute-strengthening contribution because it had a reverse effect on strength relative to EC.

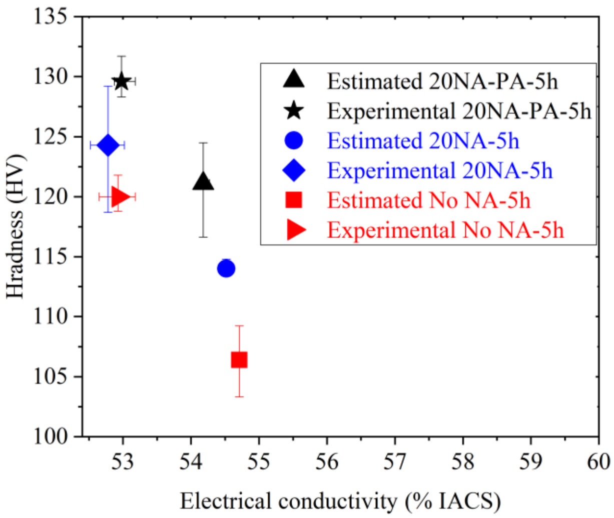

Fig. 12 Plot of the hardness vs the electrical conductivity (% IACS) for estimated and measured values for all drawn samples.

4.2. Microstructural evolution

The DSC results (Fig. 5a and 5b) demonstrate that natural aging was detrimental to the subsequent precipitation (peak I) before wire drawing. However, it was found that severe plastic deformation via cold wire drawing following natural aging could counteract the detrimental effect of natural aging, as confirmed by DSC analysis, TEM, and hardness measurements. For a better understanding, Fig. 13 presents a scheme of the microstructural evolution that occurred under various conditions.

The microstructure of the No-NA sample in the as-drawn condition comprised a forest of dislocations with no precipitates (Fig. 13a). During artificial aging, the majority of precipitation occurred along dislocations as nucleation sites [19, 20, 40]. At the peak aging condition, the preferential distribution of precipitates along dislocations was the dominant feature of the microstructure (Fig. 7a). After 5 h of aging, these precipitates became coarser and more homogenous (Fig. 7b and Fig. 13b). Two types of precipitates formed in the No-NA sample: lath-like and needle-shaped precipitates, whose crystal structures had a similar hexagonal substructure as the β' precipitates [19].

In the naturally aged 20NA samples, a large number of GP zones formed, primarily over the matrix (Fig. 13c). In the subsequent cold wire drawing, GP zones were successively sheared owing to the dislocation movement during wire drawing. It resulted in increasing interfacial energy and reducing thermal stability of the sheared GP zones. Finally, GP zones dissolved into the matrix. It appears that they were dissolved as solute-enriched aggregates (Fig. 13d) rather than homogeneously dispersed solutes, as confirmed in Ref. [13, 25, 41] using high-resolution TEM. This can be attributed to the low diffusion rate of solutes in cold wire drawing. It should be noted that the dissolution of GP zones might not be due to an increase in temperature [28] because the wire was kept cool with water during drawing. It is worth mentioning that the number of dislocations that formed during drawing was relatively similar in the drawn 20NA and No-NA samples. During the subsequent aging, in addition to the precipitates that formed along the dislocations, it is possible that other phases precipitated from the enriched aggregates [25], which could be recognized by their smaller cross section but are not yet identified in the present work (Fig. 7c and Fig. 13e). The higher and wider I_d peak in the as-drawn NA sample compared to the drawn No-NA sample could be attributed to the formation of these fine precipitates along with lath-like and needle-shaped phases (Fig. 7c and Fig. 13e). Therefore, a higher number density of precipitates was obtained in the drawn 20NA sample compared to that in the drawn No-NA sample. Large lath-like precipitates along dislocations could be connected with dislocation-assisted diffusion mechanism (Fig. 7a). Thus, rich dislocations generated during drawing could accelerate the diffusion of solute atoms during subsequent aging. Therefore, it resulted in larger lath-like precipitates [40, 42]. On the other hand, the solute-enriched aggregates in less dense dislocation zones could evolve into fine precipitates during aging. These precipitates would be less dependent on the dislocation-induced mechanism, and they might grow slowly during aging, leading to finer precipitates.

In the 20NA-PA condition, precipitation initially occurred in the non-deformed condition after 5 h of aging, and the microstructure consisted of predominant β'' precipitates along with a few β' phases. The precipitates were evenly distributed throughout the matrix (Fig. 13f). Then, wire drawing was applied to the aged samples (20NA-PA). The number of formed dislocations in the drawn 20NA-PA sample was less than that in the drawn 20NA and No-NA samples. This suggests that the strain hardening due to the solute atoms in the drawn 20NA and No-NA samples was more effective relative to the strengthening of β'' precipitates in the drawn 20NA-PA sample [25]. In the 20NA-PA sample, it was observed that precipitates were also sheared and fragmented by moving dislocations (by comparing the precipitate sizes before and after drawing, Fig. 8), leading to smaller precipitates (Fig. 13g). The number density of precipitates decreased slightly after wire drawing, which might be attributed to the re-dissolution of some β'' precipitates, as reported in Ref. [25]. After aging at 180 °C for 5 h, the precipitates were coarsened in the drawn 20NA-PA sample (Fig. 13h). It is plausible that some β'' precipitates were transformed into β' phases during the post-aging treatment.

It should be noted that precipitates in the drawn 20NA-PA sample after 5h of aging are uniformly distributed. This is because most precipitates were uniformly formed from the clusters and GP zones before wire drawing, and dislocations barely acted as a nucleation site. However, in drawn No-NA and 20NA samples, precipitation mainly took place after wire drawing, meaning that dislocation-induced precipitation could be dominant. Lath-like precipitates were mainly formed along dislocations at the peak-aged condition in drawn No-NA and 20NA samples.

As discussed in Section 3.1, the naturally aged samples showed a better combination of strength and EC relative to those of the No-NA samples. It should be noted that the strain hardening in the No-NA and 20NA samples was more or less similar, as discussed in Section 3.4. Strain hardening and precipitate strengthening were the main strengthening mechanisms in the studied samples. Thus, the higher strength of the NA samples is attributed to their higher precipitate strengthening. In addition to lath-like and needle-shaped precipitates, the 20NA sample microstructure was also characterized by the presence of smaller precipitates (Fig. 13e and Fig. 7c), which were most probably enriched aggregates.

As mentioned in Section 3.1, the 20NA-PA sample showed the highest strength above the minimum required EC among all the samples. However, the 20NA-PA sample had the lowest strain hardening contribution compared to that of the No-NA and 20NA samples, which is schematically shown in Fig. 13g by the lowest number density of dislocations. In contrast, the 20NA-PA sample possessed the greatest precipitate number density among all samples, overcoming the inferiority of strain hardening in the 20NA-PA sample.

Solutes and precipitates were the major sources of electrical resistivity, controlling the total resistivity. As pointed out in Section 4.1, the solutes caused more electrical resistivity compared to precipitates in the studied samples. Given that 20NA-PA had the highest precipitate number density, it could be deduced that the electrical resistivity of the precipitates in the 20NA-PA sample was comparatively higher than that in the No-NA and 20NA samples. Considering that the EC (53% IACS) was similar for all samples (3.25×10^{-6} Ω cm), it can be concluded that the solute resistivity in the 20NA-PA sample might be relatively lower than that in the No-NA and 20NA samples.

5. Conclusions

1. Natural aging combined with wire drawing (in the 10NA and 20NA samples) was found to be favorable. The natural aging samples exhibited a higher strength at a given electrical conductivity upon subsequent aging treatment compared to the samples without natural aging.

2. Natural aging combined with pre-aging (in the 20NA-PA sample) showed the highest strength above 52.5% IACS among all samples, which was higher than the strength values defined in the EN 50183 standard.
3. The higher strength of the 20NA-PA sample aged for 5 h mainly stemmed from the larger portion of precipitate strengthening. However, its dislocation hardening was smaller than that of the no natural aging and 20NA samples because solutes exhibited a stronger effect on strain hardening than shearable precipitates.
4. The pre-aging treatment prior to wire drawing maximized precipitate strengthening.
5. The relationship between strength and electrical conductivity was analyzed in detail using strengthening models and Matthiessen's rule. This approach is believed to provide a reasonable explanation for the mechanical and electrical properties of drawn Al–Mg–Si conductor alloys.

Acknowledgements

The authors would like to acknowledge the financial support of the Natural Sciences and Engineering Research Council of Canada (NSERC) under the Grant No. CRDPJ 514651-17 and Rio Tinto Aluminum through the Research Chair in the Metallurgy of Aluminum Transformation at the University of Quebec in Chicoutimi.

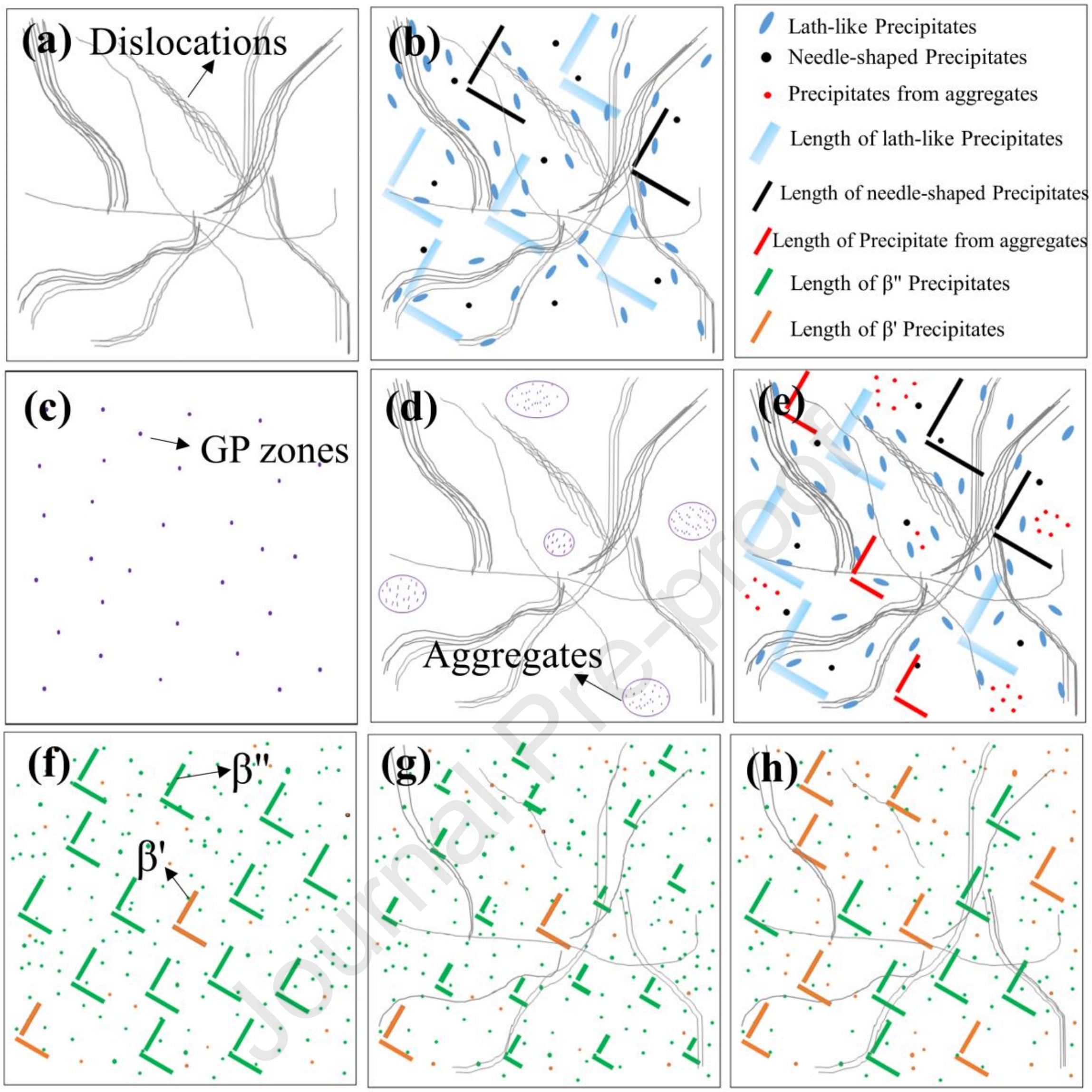

Figure 13 Sketches to illustrate the microstructural evolution in the samples with NA and PA compared to the conventional sample (No-NA) before and after aging treatment: (a) as-drawn No-NA sample, (b) drawn No-NA sample after 5 h aging, (c) GP zones in 20NA sample prior to wire drawing, (d) as-drawn 20NA sample, (e) drawn 20NA sample aged for 5 h, (f) 20NA-PA before wire drawing, (g) as-drawn 20NA-PA sample, and (f) drawn 20NA-PA aged for 5 h.

Credit authorship contribution statement:

Siamak Nikzad Khangholi: Methodology, Investigation, Formal analysis, Writing – original draft. Mousa Javidani: Conceptualization, Methodology, Writing – review & editing. Alexandre Maltais: Conceptualization, Validation, Writing – review & editing. X.-Grant Chen: Conceptualization, Validation, Writing – review & editing, Project administration.

Data availability

The raw/processed data required to reproduce these findings cannot be shared at this time as the data also forms part of an ongoing study.

References

[1] S. Karabay, Influence of AlB_2 compound on elimination of incoherent precipitation in artificial aging of wires drawn from redraw rod extruded from billets cast of alloy AA-6101 by vertical direct chill casting, Materials & Design 29(7) (2008) 1364-1375.
[2] S. Karabay, Modification of AA-6201 alloy for manufacturing of high conductivity and extra high conductivity wires with property of high tensile stress after artificial aging heat treatment for all-aluminium alloy conductors, Materials & Design 27(10) (2006) 821-832.
[3] M.G. E. Cervantes, J. A. Ramos, S.A. Montes, Influence of Natural Aging and Cold Deformation on the Mechanical and Electrical Properties of 6201-T81 Aluminum Alloy Wires, Mater. Res. Soc. Symp. Proc, 2010, pp. 03-09.
[4] Y. Han, D. Shao, B.A. Chen, Z. Peng, Z.X. Zhu, Q. Zhang, X. Chen, G. Liu, X.M. Li, Effect of Mg/Si ratio on the microstructure and hardness–conductivity relationship of ultrafine-grained Al–Mg–Si alloys, Journal of Materials Science 52(8) (2016) 4445-4459.
[5] R.Z. Valiev, M.Y. Murashkin, I. Sabirov, A nanostructural design to produce high-strength Al alloys with enhanced electrical conductivity, Scripta Materialia 76 (2014) 13-16.
[6] S. Jiang, R. Wang, Grain size-dependent Mg/Si ratio effect on the microstructure and mechanical/electrical properties of Al-Mg-Si-Sc alloys, Journal of Materials Science & Technology 35(7) (2019) 1354-1363.
[7] B. Raeisinia, W.J. Poole, D.J. Lloyd, Examination of precipitation in the aluminum alloy AA6111 using electrical resistivity measurements, Materials Science and Engineering: A 420(1) (2006) 245-249.
[8] X. Sauvage, E.V. Bobruk, M.Y. Murashkin, Y. Nasedkina, N.A. Enikeev, R.Z. Valiev, Optimization of electrical conductivity and strength combination by structure design at the nanoscale in Al–Mg–Si alloys, Acta Materialia 98 (2015) 355-366.
[9] R.M. Mustafa, Production of aluminium-silicon-magnesium wrought alloy rod with application in the manufacture of extra-high conductivity AAAC for overhead electrical transmission lines, Light Metals, 2008, pp. 613-617.
[10] ASM Handbook: Casting. Volume 15, ASM International, 1998, pp. 689-690.
[11] D. Lindholm, S. Akhtar, D. Mortensen, Numerical Simulation of Wire Rod Casting of AA1370 and AA6101 Alloys, Light Metals 20202020, pp. 1032-1038.

[12] P.A. Rometsch, Z. Xu, H. Zhong, H. Yang, L. Ju, X.H. Wu, Strength and Electrical Conductivity Relationships in Al-Mg-Si and Al-Sc Alloys, Materials Science Forum 794-796 (2014) 827-832.
[13] G. Lin, Z. Zhang, H. Wang, K. Zhou, Y. Wei, Enhanced strength and electrical conductivity of Al–Mg–Si alloy by thermo-mechanical treatment, Materials Science and Engineering: A 650 (2016) 210-217.
[14] C.H. Liu, J. Chen, Y.X. Lai, D.H. Zhu, Y. Gu, J.H. Chen, Enhancing electrical conductivity and strength in Al alloys by modification of conventional thermo-mechanical process, Materials & Design 87 (2015) 1-5.
[15] C. Bunte, M. Glassel, C. Medina, D. Zalcman, Proposed Solution for Random Characteristics of Aluminium Alloy Wire Rods Due to the Natural Aging, Procedia Materials Science 9 (2015) 97-104.
[16] L.M. Cheng, W.J. Poole, J.D. Embury, D.J. Lloyd, The influence of precipitation on the work-hardening behavior of the aluminum alloys AA6111 and AA7030, Metallurgical and Materials Transactions A 34(11) (2003) 2473-2481.
[17] J. Buha, R.N. Lumley, A.G. Crosky, K. Hono, Secondary precipitation in an Al–Mg–Si–Cu alloy, Acta Materialia 55(9) (2007) 3015-3024.
[18] G.A. Edwards, K. Stiller, G.L. Dunlop, M.J. Couper, The precipitation sequence in Al–Mg–Si alloys, Acta Materialia 46(11) (1998) 3893-3904.
[19] K. Teichmann, C.D. Marioara, S.J. Andersen, K.O. Pedersen, S. Gulbrandsen-Dahl, M. Kolar, R. Holmestad, K. Marthinsen, HRTEM study of the effect of deformation on the early precipitation behaviour in an AA6060 Al–Mg–Si alloy, Philosophical Magazine 91(28) (2011) 3744-3754.
[20] R.S. Yassar, D.P. Field, H. Weiland, The effect of predeformation on the β″ and β′ precipitates and the role of Q′ phase in an Al–Mg–Si alloy; AA6022, Scripta Materialia 53(3) (2005) 299-303.
[21] H. Nemour, D. Mourad Ibrahim, A. Triki, The effect of heavy cold plastic deformation on the non-isothermal kinetics and the precipitation sequence of metastable phases in an Al–Mg–Si alloy, Journal of Thermal Analysis and Calorimetry 123(1) (2015) 19-26.
[22] G. Höhne, W. Hemminger, H.J. Flammersheim, Differential Scanning Calorimetry: An Introduction for Practitioners, Springer-Verlag1996.
[23] O. Engler, C.D. Marioara, Y. Aruga, M. Kozuka, O.R. Myhr, Effect of natural ageing or pre-ageing on the evolution of precipitate structure and strength during age hardening of Al–Mg–Si alloy AA 6016, Materials Science and Engineering: A 759 (2019) 520-529.
[24] E. Standard, EN 50183. Conductors for overhead lines, aluminium magnesium silicon alloy wires, (2000), 4-9.
[25] H. Li, M. Qingzhong, Z. Wang, F. Miao, B. Fang, R. Song, Z. Zheng, Simultaneously enhancing the tensile properties and intergranular corrosion resistance of Al–Mg–Si–Cu alloys by a thermo-mechanical treatment, Materials Science and Engineering: A 617 (2014) 165-174.
[26] H.W.Z. S.J. Andersen, J. Jansen, C. TrÆholt, U. Tundal, O. Reiso, The crystal structure of the β″ phase in Al–Mg–Si alloys, Acta Materialia, 1998, pp. 3283-3298.
[27] M.Y.M. X. Sauvage, R. Z. Valiev, Atomic scale investigation of dynamic precipitation and grain boundary segregation in a 6061 aluminium alloy nanostructured by ECAP, Kovove Mater. 49, 2011, pp. 11-15.
[28] M. Murayama, Z. Horita, K. Hono, Microstructure of two-phase Al–1.7 at% Cu alloy deformed by equal-channel angular pressing, Acta Materialia 49(1) (2001) 21-29.

[29] T. Ye, L. Li, P. Guo, G. Xiao, Z. Chen, Effect of aging treatment on the microstructure and flow behavior of 6063 aluminum alloy compressed over a wide range of strain rate, International Journal of Impact Engineering 90 (2016) 72-80.
[30] W.-S. Lee, J.-C. Shyu, S.-T. Chiou, Effect of strain rate on impact response and dislocation substructure of 6061-T6 aluminum alloy, Scripta Materialia 42(1) (1999) 51-56.
[31] L.F. Deschamps A, Brechet Y, Influence of predeformation on ageing in an Al-Zn-Mg alloy-I. Microstructure evolution and mechanical properties, Acta Materialia, 1998, pp. 281-292.
[32] J.G. Kaufman, Introduction to Aluminum Alloys and Tempers, ASM International, (2000) 39-41.
[33] Y.J. Li, A.M.F. Muggerud, A. Olsen, T. Furu, Precipitation of partially coherent α-Al(Mn,Fe)Si dispersoids and their strengthening effect in AA 3003 alloy, Acta Materialia 60(3) (2012) 1004-1014.
[34] J. Zhang, M. Ma, F. Shen, D. Yi, B. Wang, Influence of deformation and annealing on electrical conductivity, mechanical properties and texture of Al-Mg-Si alloy cables, Materials Science and Engineering: A 710 (2018) 27-37.
[35] K. Li, A. Béché, M. Song, G. Sha, X. Lu, K. Zhang, Y. Du, S.P. Ringer, D. Schryvers, Atomistic structure of Cu-containing β ″precipitates in an Al–Mg–Si–Cu alloy, Scripta Materialia 75 (2014) 86-89.
[36] S. Nikzad Khangholi, M. Javidani, A. Maltais, X.G. Chen, Optimization of mechanical properties and electrical conductivity in Al–Mg–Si 6201 alloys with different Mg/Si ratios, Journal of Materials Research 35(20) (2020) 2765-2776.
[37] J.P. Hou, Q. Wang, Z.J. Zhang, Y.Z. Tian, X.M. Wu, H.J. Yang, X.W. Li, Z.F. Zhang, Nano-scale precipitates: The key to high strength and high conductivity in Al alloy wire, Materials & Design 132 (2017) 148-157.
[38] W. Wen, Y. Zhao, J.G. Morris, The effect of Mg precipitation on the mechanical properties of 5xxx aluminum alloys, Materials Science and Engineering: A 392(1-2) (2005) 136-144.
[39] ASTM B193, Annual Book of ASTM Standards, Electrical Conductors, (2002) 3-4.
[40] M. Kolar, K.O. Pedersen, S. Gulbrandsen-Dahl, K. Marthinsen, Combined effect of deformation and artificial aging on mechanical properties of Al–Mg–Si Alloy, Transactions of Nonferrous Metals Society of China 22(8) (2012) 1824-1830.
[41] Z. Wang, H. Li, F. Miao, B. Fang, R. Song, Z. Zheng, Improving the strength and ductility of Al–Mg–Si–Cu alloys by a novel thermo-mechanical treatment, Materials Science and Engineering: A 607 (2014) 313-317.
[42] R. Lu, S. Zheng, J. Teng, J. Hu, D. Fu, J. Chen, G. Zhao, F. Jiang, H. Zhang, Microstructure, mechanical properties and deformation characteristics of Al-Mg-Si alloys processed by a continuous expansion extrusion approach, Journal of Materials Science & Technology 80 (2021) 150-162.

Declaration of interests:

☒ The authors declare that they have no known competing financial interests or personal relationships that could have appeared to influence the work reported in this paper.

☐~~The authors declare the following financial interests/personal relationships which may be considered as potential competing interests:~~